Annu. Rev. Phys. Chem. 1993. 44: 237–63
Copyright © 1993 by Annual Reviews Inc. All rights reserved

SCANNING TUNNELING MICROSCOPY STUDIES OF LOW-DIMENSIONAL MATERIALS: Charge Density Wave Pinning and Melting in Two Dimensions

Hongjie Dai and Charles M. Lieber

Department of Chemistry and Division of Applied Sciences, Harvard University, Cambridge, Massachusetts 02138

KEY WORDS: impurity pinning, phase transition, hexatic phase, superconductivity

INTRODUCTION

A major goal of current efforts in condensed matter research is to understand the factors that determine the structure, electronic properties, and phase transitions in materials, as such knowledge will lead the way to the rational design of new solids with predictable properties (1, 2). Essential to the achievement of this goal is a detailed understanding of how material properties vary and can be controlled by atomic level modifications, such as substitutional doping. In principle, doping is a straightforward process with readily predictable effects (e.g. doping semiconductors). However, in many materials, especially those that exhibit cooperative phenomena, such as charge density waves (CDW) and superconductivity, the role of dopants and impurities is not well understood (3, 4). Past difficulties in elucidating the microscopic effects of dopants and impurities on material properties can be traced to the fact that conventional diffraction and spectroscopic techniques provide only an averaged view of a solid (5). These techniques have not been able to assess unambiguously structural disorder and electronic inhomogeneity in doped solids (3, 4, 6).

0066–426X/93/1101–0237$05.00

To characterize the electronic and structural properties of doped materials at the atomic level, we have been using scanning tunneling microscopy (STM) (3, 4, 6–20). STM is now a relatively mature technique that can be used to probe surface structure and electronic states directly on the atomic scale (21–26). Although STM is a surface sensitive technique, it can also provide information essential to understanding bulk material properties: If a cleaved crystal surface does not reconstruct, then the structure and electronic properties of the interface are often representative of the bulk. Highly anisotropic materials (i.e. low-dimensional solids) typically have low free energy surfaces that do not reconstruct; hence, surface-sensitive STM studies of these systems can provide detailed information relevant to their bulk properties. The investigation of low-dimensional materials with STM is not, however, a contrived problem, as large material anisotropy is essential to the exciting phenomena, such as CDW and high-temperature superconductivity, that these systems exhibit.

In our discussion, we focus on STM studies of the CDW state in the quasi-two-dimensional material tantalum disulfide, TaS_2. The scope of the review is as follows: First we introduce key features of the tunneling microscope and the theoretical concepts needed to interpret the experimental data. We then review CDWs in metal-substituted TaS_2, including a theoretical treatment of the CDW-impurity interaction. Finally, we focus on experimental results, including STM images of CDWs in niobium-doped TaS_2, topological defects in the CDW lattice, an analysis of two-dimensional order in this system, and the implications of these results to the general phenomena of two-dimensional melting and impurity pinning.

BACKGROUND

Scanning Tunneling Microscopy

In this section, we briefly review the instrumentation and theoretical concepts that are essential for understanding the STM studies discussed below. More detailed reviews can be found elsewhere (21–26). A typical microscope is illustrated schematically in Figure 1. The underlying basis for the operation of the microscope is electron tunneling between a sharp metal tip and a conducting sample. When the tip and sample are brought sufficiently close, their wave functions can overlap. If a bias voltage V is then applied to the sample, a tunneling current I will flow between the sample and tip. Electrons will tunnel from filled electronic states in the tip to empty states in the sample when V is positive; conversely, electrons will tunnel from filled sample states to empty tip states when V is negative (Figure 1). The tunneling current that flows when V is applied varies exponentially with the tip-sample separation. For a typical work function of 4 eV, I decreases

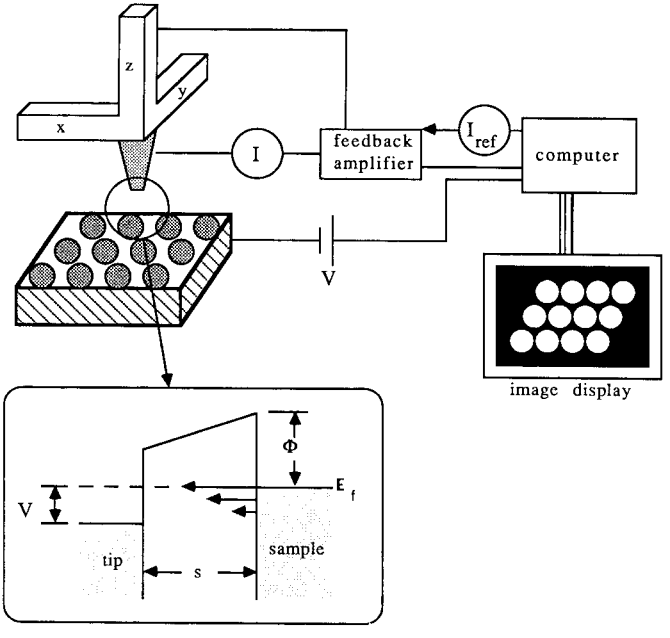

Figure 1 Schematic view of a tunneling microscope. The inset is a one-dimensional representation of tunneling between a metallic tip and sample, where s is the tip-sample separation and V is the applied voltage.

ten-fold for an angstrom increase in separation. The strong exponential dependence of the tunneling current on distance enables STM to achieve high vertical resolution. An atomic resolution map of the surface can then be generated by rastering the tip over the sample with angstrom level control that is possible with piezoceramic positioners. Experimental images are typically acquired in the constant current mode in which a feedback loop controls the vertical position of the tip above the sample so that I is equal to a reference current (I_{ref}) at all coordinates on the surface. Features in constant current mode images thus correspond to vertical displacements of the positioner needed to maintain a constant tunneling current.

To interpret such STM data, we must understand the response of the tunneling current to the barrier properties, applied voltage, etc.; insight into these problems can be obtained from analyses of the tunneling problem (27–31). As first discussed by Tersoff & Hamann (27), an expression for I can be readily derived by assuming free sample and tip wave functions, and then using perturbation theory. In the limit of small bias voltage and low temperature, this treatment yields

$$I = (2\pi/\hbar)e^2 V \sum |M_{st}|^2 \delta(E_s - E_f)\delta(E_t - E_f) \quad 1.$$

where M_{st} is the tunneling matrix element between wave functions on the tip ψ_t and sample ψ_s, and E_f is the Fermi energy. As shown by Bardeen (32), the tunneling matrix element can be written as

$$M_{st} = (\hbar^2/2m) \int (\psi_t^* \nabla \psi_s - \psi_s \nabla \psi_t^*)\, dS \quad 2.$$

where the integral corresponds to a surface within the barrier region between the sample and tip. To evaluate M_{st} in a way that the resulting expression for I can be compared quantitatively with STM images in general (i.e. not for one specific choice of sample and tip) requires several approximations. Tersoff & Hamann showed that by assuming the tip forms a locally spherical potential well with only s wave functions, I could be expressed as

$$I\alpha \sum_s |\psi_s(r_o)|^2 \delta(E_s - E_f). \quad 3.$$

By definition, the summation is the local density of sample electronic states, $\rho(r_o, E)$, at the center of curvature of the tip

$$\rho(r_o, E) \equiv \sum_s |\psi_s(r_o)|^2 \delta(E_s - E_f). \quad 4.$$

Thus, constant current images correspond to contours of constant density of sample electronic states. Because a CDW causes a variation of the electronic states close to the E_f, STM represents a uniquely sensitive and direct probe of the structure and amplitude of the CDW lattice. Below, we introduce the TaS_2 system and a detailed background to CDWs.

Metal-Doped Tantalum Disulfide

Tantalum disulfide is a layered material that consists of strongly bonded sulfur-tantalum-sulfur layers that are held together by van der Waals forces between adjacent hexagonal close packed sulfur planes (Figure 2; 33–35). Electronically, one would expect that the partially filled t_{2g} conduction band in this d^1 system would give rise to metallic conduction. At high temperatures, TaS_2 is metallic; however, on cooling below 543 K, TaS_2 exhibits four distinct temperature dependent CDW states (34, 35). In general, CDWs are found in low-dimensional systems that exhibit significant Fermi surface nesting, where nesting refers to the condition in which a piece of Fermi surface may be translated and superimposed onto another piece by a wave vector $\mathbf{q}$. Fermi surface nesting leads to a divergence in the electronic susceptibility at the wave vector $\mathbf{q}$ and, through

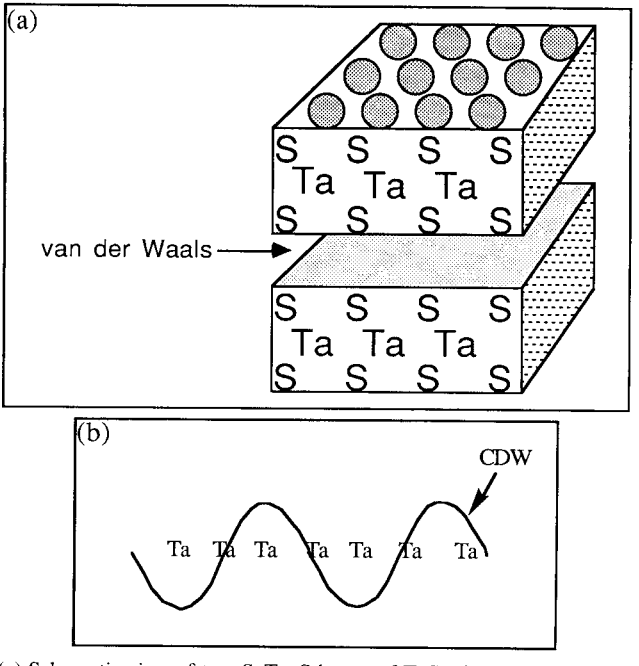

Figure 2 (*a*) Schematic view of two S–Ta S layers of TaS_2 that are bonded primarily via dispersion forces. The sulfur atoms are arranged in hexagonal close packed planes. (*b*) One-dimensional view of a sinusoidal CDW in a single S Ta–S layer.

electron-phonon coupling, can yield a stable periodic modulation of the lattice and conduction electron density, i.e. a CDW. The periodicity or wavelength (λ) of the CDW is governed by $\mathbf{q}$. Because λ is determined by the Fermi surface size through $\mathbf{q}$, it may not correspond to an integral number of lattice constants ($n\mathbf{a}$). In the case where $\lambda \neq n\mathbf{a}$, the CDW is called incommensurate; however, when $\lambda = n\mathbf{a}$, it is termed commensurate.

Before the advent of STM, the structure of the CDW phases in TaS_2 and other materials had been investigated by x-ray and electron diffraction. These techniques showed that in TaS_2 the high temperature CDW was incommensurate, and that for $T < 183$ K the CDW rotated 13.9° relative to the atomic lattice to become commensurate (34–36). Unfortunately, the structures of the two intermediate temperature CDW phases could not be resolved by using diffraction techniques. This situation has changed substantially, since Coleman et al (37) demonstrated that STM could directly image a CDW. The ability of STM to determine CDW and atomic lattice positions simultaneously has subsequently been exploited by us (3, 7–13, 38, 39) and others (40–43) to resolve the complicated structural details of the intermediate temperature CDW phases in TaS_2. These data

have significantly increased our understanding of the physics of this material.

Here, we concentrate on a more general problem that has significant chemical implications; that is, to understand how a CDW interacts with metal impurities doped into the atomic lattice. Understanding the nature of the interaction between impurities and a CDW is essential to understanding the static and dynamic properties of the CDW state (44–51), and the design of a modified material that has predictable properties. In general, pinning can be defined as either strong or weak, depending on the competing energetics of the CDW-impurity interaction and the CDW deformation energy (44, 45, 47, 48). In strong pinning, the impurity potential dominates the CDW elastic energy and pins the phase of the CDW at each impurity site. In weak pinning, the CDW breaks up into constant phase regions that are pinned collectively by impurities. Despite the fundamentally different structural manifestations of strong and weak pinning, there has been considerable controversy concerning the nature of pinning in CDW systems (11, 13, 44–55). This controversy has largely been due to the lack of data characterizing the evolution of CDW structure with impurity doping. Real-space imaging of the CDW structure in doped materials by STM can, however, address directly the essential issue of strong versus weak pinning (8, 9, 11–13).

In addition, an important and general consequence of pinning is structural disorder. In two-dimensional systems, disorder can manifest itself in intriguing ways (56–61). For example, Halperin and Nelson (57, 58) predicted that a two-dimensional solid can melt in a continuous transition through a hexatic state that is characterized by long-range orientational order and exponentially decaying positional order. This unique hexatic state arises from the formation of topological defects in the lattice. Disorder due to impurity pinning has many similarities to melting, although melting theory (57–59) is based upon equilibrium thermal disorder, whereas pinning is typically a quenched disorder. Because statistical averaging differs for equilibrium and quenched disorder (62), it is also important to examine carefully the analogy of disorder in pinned systems to equilibrium theory; we discuss these concepts in detail below.

CDW Pinning

The one-dimensional Fukuyama-Lee-Rice (FLR) CDW pinning model (47, 48) has been the starting point for many studies of CDW-impurity pinning. In the FLR model, the electron density distribution $\rho(\mathbf{r})$ is treated as a sinusoidal wave with a constant amplitude ρ_0 modulated over a uniform background electron density ρ_{av}:

$$\rho(\mathbf{r}) = \rho_{av} + \rho_0 \cos[\mathbf{Q}\cdot\mathbf{r} + \phi(\mathbf{r})]. \qquad 5.$$

The wave vector of the CDW is $\mathbf{Q} = 2\mathbf{k}_f$, and the real-space periodicity of the electron density is $\pi/\mathbf{k}_f$. The FLR model treats the impurity-CDW interaction within a Ginzburg-Landau framework, in which the order parameter is the CDW phase, $\phi(\mathbf{r})$. For a perfect CDW free of impurities, $\phi(\mathbf{r})$ is a constant. Interestingly, if $\phi(\mathbf{r})$ is constant and the wave vector $\mathbf{Q}$ is incommensurate with the atomic lattice, then the energy of the CDW state is independent of its position relative to the atomic lattice (63).

However, $\phi(\mathbf{r})$ may vary with position when impurities are introduced into the host atomic lattice, because impurities can pin the CDW phase. To calculate the expected behavior of the CDW in the presence of impurities, we consider several limiting cases for a one-dimensional system. In the commensurate state ($\mathbf{Q} = 2\pi/n\mathbf{a}$) the CDW is in registry with the atomic lattice and is thus strongly pinned to the atomic lattice. Impurity pinning does not perturb significantly the commensurate CDW state (64). On the other hand, an incommensurate CDW ($\mathbf{Q} \neq 2\pi/n\mathbf{a}$) interacts weakly with the underlying lattice. Variations in the lattice potential due to impurity atoms can thus effectively distort or pin an incommensurate CDW. Qualitatively, an attractive pinning potential will distort CDW maxima toward the nearest impurities to minimize the energy. The interaction of the impurities with the incommensurate CDW is examined below.

First, we assume that each impurity has a short-ranged pinning potential and that this potential has the same magnitude for every impurity. The total pinning potential distribution is thus a function of the positions of the randomly quenched impurities:

$$V_{\text{pin}}(\mathbf{r}) = V_o \sum_i \delta(\mathbf{r} - \mathbf{R}_i) \qquad 6.$$

where $\mathbf{R}_i$ is the ith impurity position vector, and the sum is over all impurities.

Similar to other solids, the CDW lattice has rigidity that can be quantified by the elastic constant $\kappa \approx \hbar v_f / A_0$, where A_0 is the unit cell area (65). Because a distortion of the CDW lattice from equilibrium will cost the system elastic energy, we must account for pinning and CDW rigidity simultaneously. This is accomplished by computing the potential energy gain associated with pinning and the elastic energy loss due to CDW distortions by using the following effective Hamiltonian:

$$H = \int \rho(\mathbf{r}) V_{\text{pin}}(\mathbf{r}) \mathrm{d}^d\mathbf{r} + \frac{\kappa}{2} \int [\nabla\phi(\mathbf{r})]^2 \, \mathrm{d}^d\mathbf{r}. \qquad 7.$$

The first term is the pinning energy, the second term is the elastic energy,

and d is the dimensionality of the system. Combining Equations 5, 6, and 7 yields

$$H = \rho_0 v_o \sum_i \cos\left[\mathbf{Q}\cdot\mathbf{R}_i + \phi(\mathbf{R}_i)\right] + \frac{\kappa}{2}\int \left[\nabla\phi(\mathbf{r})\right]^2 \mathrm{d}^d\mathbf{r}. \qquad 8.$$

The pinning energy depends on the random impurity configuration, and the elastic energy depends on the CDW phase fluctuations caused by pinning.

The phase variation is determined by minimizing the total energy. Two limiting cases, strong and weak pinning, are considered. In the strong pinning regime, the elastic energy is much less than the pinning potential. Hence, the CDW phase is pinned to each impurity site with the phase given by $\mathbf{QR}_i + \phi(\mathbf{R}_i) = -\pi$ (Figure 3). The energy determined for the limiting case of strong pinning is then $-\rho_0|V_o|N_i$, where N_i is the total number of impurities, i.e., the energy is simply proportional to the number of impurities. On the other hand, in the weak pinning regime the pinning energy is much smaller than the energy required to deform the CDW. Hence, phase distortions do not occur at each impurity site $[\mathbf{QR}_i + \phi(\mathbf{R}_i) \neq -\pi]$; rather, $\phi(\mathbf{r})$ varies on a length scale much larger than the impurity spacing (Figure 3). Because each term in the sum in Equation 8 can be either positive or negative, the total pinning energy grows only as $N_i^{1/2}$ (versus N_i for strong pinning). An interesting consequence of the FLR weak pinning model is that the CDW will be unstable to domain formation for $d < 4$. These domains should consist of distinct regions containing many impurities within which the CDW phase varies smoothly. The STM studies described below provide a unique test of this prediction.

Quantitatively, a parameter ε is used to characterize the pinning strength and separate the strong and weak pinning regimes:

$$\varepsilon = \frac{\rho_0 V_o}{\kappa \cdot n_i^{2/d-1}} \qquad 9.$$

where $\rho_0 V_o$ is the pinning potential energy per impurity, and $\kappa \cdot n_i^{2/d-1}$ is the dimensionality dependent elastic energy per impurity (65). Hence, $\varepsilon \gg 1$ corresponds to the strong pinning regime, and $\varepsilon \ll 1$ corresponds to the weak pinning regime.

As indicated above, approximately constant phase domains containing many impurities are expected in the weakly pinning regime. The length scale of these domains can be estimated by using the scaling arguments of Imry & Ma (66). Specifically, they showed that the pinning energy scales as $L^{d/2}$, whereas the elastic energy scales as L^{d-2}. Hence, the pinning energy gain is $\rho_0 V_o N_i^{1/2} = \rho_0 V_o n_i^{1/2} L^{d/2}$, and the elastic energy cost is κL^{d-2}

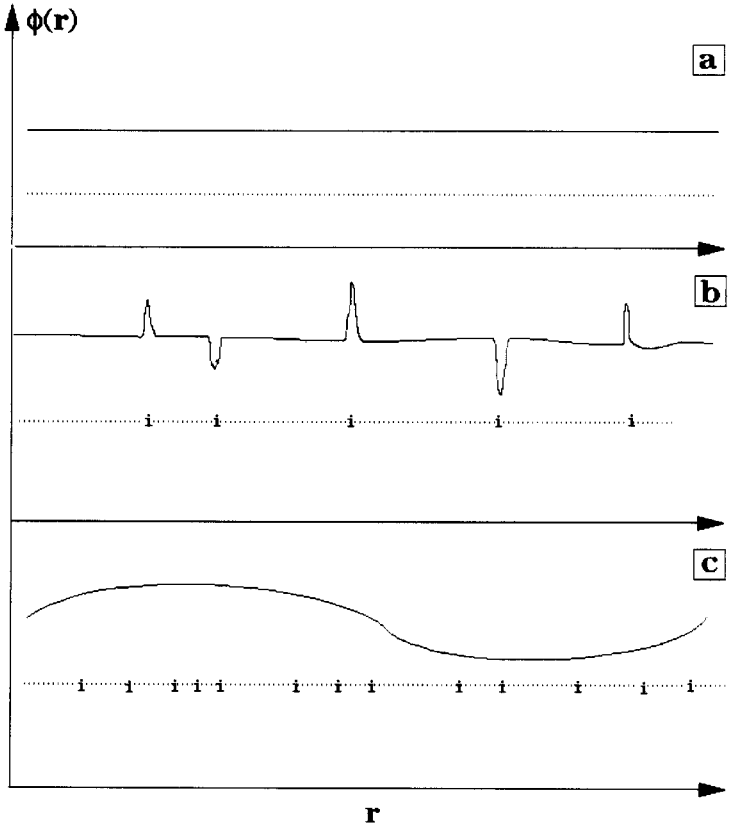

Figure 3 Plots of the CDW phase, $\phi(\mathbf{r})$, versus position for (*a*) a perfect one-dimensional lattice and (*b*, *c*) for lattices that contain impurities, i. The abrupt variation in $\phi(\mathbf{r})$ at each impurity site (*b*) corresponds to strong pinning. The smooth variation in $\phi(\mathbf{r})$ over a distance containing several impurities (*a*) corresponding to weak pinning.

[assume $\phi(\mathbf{r})$ varies by $\sim\pi$ over length L]. We can thus define a critical length L_c, which defines the average size of constant phase domains, by minimizing the energy with respect to L:

$$L_c = \alpha \cdot \frac{1}{\varepsilon} \cdot d_i, \qquad 10.$$

where α is of order unity and $d_i = n_i^{-1/d}$ is the average impurity spacing.

Specific defects in the CDW lattice arising from CDW-impurity pinning have also been studied theoretically. For example, McMillan (64) showed that the energy cost for a single dislocation diverges logarithmically with

the size of the sample; this behavior is similar to that of a dislocation in ordinary solid. The existence of dislocations can be explained by using the scaling argument outlined above. First, a dislocation loop with size L will contain $n_i L^d$ impurities. The pinning energy gain is $\sim \rho_0 V_0 n_i^{1/2} L^{d/2}$, and the elastic energy cost for creating the dislocation is $\sim \kappa$ up to a logarithm (64, 67). Because the total energy is the same as in the treatment of domains, we can obtain the critical length given by Equation 10. In the case of dislocations, L_c is comparable to the average separation between dislocation.

Lastly, the FLR model only considers phase fluctuations of the CDW; amplitude fluctuations of the CDW are ignored. A justification for ignoring amplitude fluctuations is that the energy cost for an amplitude fluctuation is significantly higher than that of the long wavelength phase fluctuations treated by FLR. Coppersmith (49) recently demonstrated, however, that amplitude fluctuations do have nontrivial effects on the CDW state. Hence, we believe that the relative importance of phase and amplitude fluctuations is an area that requires additional theoretical and experimental study.

RESULTS AND DISCUSSION

STM Results

We have investigated the effect of impurities through systematic studies of metal-substituted tantalum disulfide, $M_x Ta_{1-x}S_2$, where M atoms randomly replace Ta sites in the lattice (3, 7–13). Here, we review studies of niobium-substituted tantalum disulfide, $Nb_x Ta_{1-x}S_2$. Substitution of isoelectronic Nb(IV) for Ta(IV) represents the weakest perturbation on the potential that is possible with metal substitution, and thus serves as the best test of the weak pinning regime (11, 13, 68). The effect of Nb-substitution on the macroscopic transport properties of these $Nb_x Ta_{1-x}S_2$ materials have been assessed by variable-temperature resistivity measurements (Figure 4). In general, it is well established (3, 35, 46) that Nb-substitution (and other metal substitutions) decreases the transition temperature from the high-temperature incommensurate (IC) CDW state to the lower temperature, nearly commensurate state. Qualitatively, the suppression in the transition temperature can be rationalized by assuming that the IC state is stabilized by impurity pinning. Macroscopic measurements do not, however, address the fundamental details of pinning outlined above. To develop a microscopic understanding of the CDW-impurity interaction, we turn to STM studies of the CDW state in these materials.

High resolution STM images of the $Nb_x Ta_{1-x}S_2$ materials are shown in Figures 5–7. Images of the IC CDW phase of undoped TaS_2 samples (11, 13) exhibit a well-ordered hexagonal structure. In contrast, substitution of

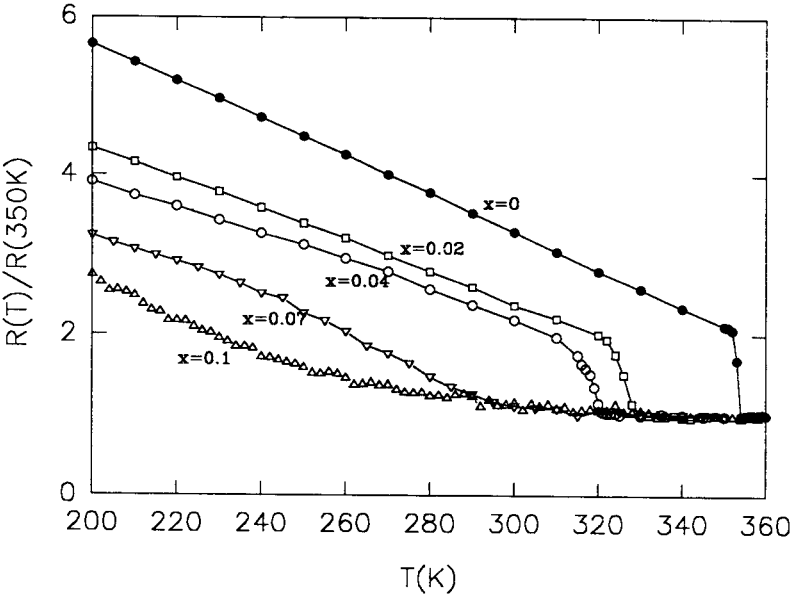

Figure 4 Normalized resistance versus temperature curves recorded on the $Nb_xTa_{1-x}S_2$ materials.

Nb causes disorder in the IC CDW lattice (Figures 5–7). The images of the Nb-doped materials exhibit areas in which the CDW lattice has hexagonal order and regions containing defects. These defects introduce disorder into the CDW lattice. The predominant defects observed in the $x(\text{Nb}) < 0.07$ samples are dislocations, which are formed by the insertion of extra half rows of CDW sites in the lattice; black lines in Figure 5*a* highlight the creation of two dislocations in a $x(\text{Nb}) = 0.02$ sample. Importantly, there is a significant strain field associated with the dislocations (67). The CDW can relax the strain field by locally deforming through site positional shifts and rotations (Figure 5*a*), although these deformations introduce disorder into the lattice. We have also found one or more CDW site vacancies close to the dislocation core in many of the images (Figure 5*b*). This latter observation is interesting, as it is completely analogous to the classical behavior of vacancies and dislocations in the atomic lattice of materials (67). Because STM can be used to study directly such defects, we believe that it will be interesting in the future to explore the generality of the $M_xTa_{1-x}S_2$ materials as models for the behavior of crystal defects and the dynamics of vacancy/dislocation formation.

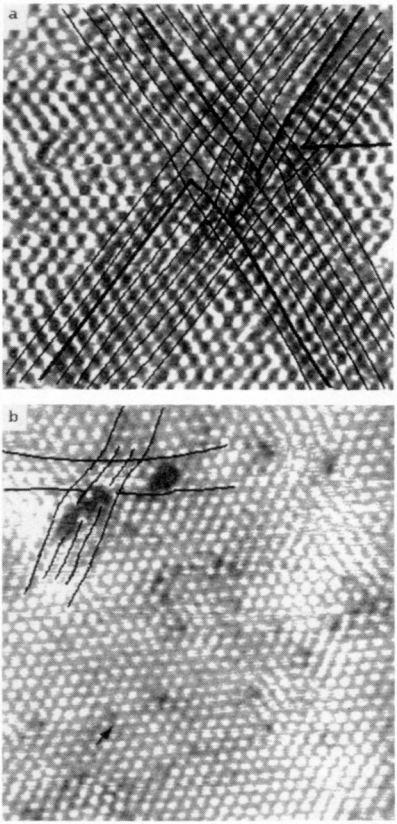

Figure 5 STM images of the incommensurate CDW state in $Nb_{0.02}Ta_{0.98}S_2$. Black lines highlight the insertion of an extra row of CDW maxima. The extra rows in (*a*) are highlighted with heavy black lines. Vacancies are also seen in (*b*).

As the impurity concentration increases to $x(\mathrm{Nb}) = 0.04$, a higher density of defects (predominantly dislocations) is observed in the CDW lattice (Figure 6). The CDW rows near the dislocations are distorted, as discussed above. However, in areas free of dislocations, the CDW lattice is locally ordered. We have highlighted several dislocation cores by constructing Burgers loops (Figure 6), which consist of equal numbers of steps along each lattice direction; a loop will remain open if it encloses a single dislocation. The vector pointing from start to end of the loop, the Burgers vector, uniquely defines the dislocation (67). We find that the Burgers vectors defining the CDW dislocations in the Nb-doped samples occur along each of the three crystallographic axes; thus, impurity-induced dislocations apparently occur randomly in the CDW lattice. In the samples containing higher impurity concentrations, $x(\mathrm{Nb}) = 0.07$ and 0.10, the STM images exhibit extended defects (Figure 7). The CDW lattice in these

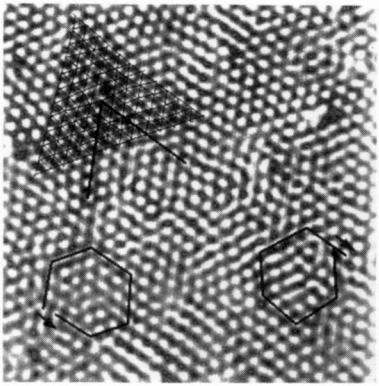

Figure 6 STM images of the incommensurate CDW state in $Nb_{0.04}Ta_{0.96}S_2$. Black lines highlight the insertion of extra rows of CDW maxima in the lattice. Two distinct Burgers loops and Burgers vectors are drawn in to highlight dislocations in the CDW lattice.

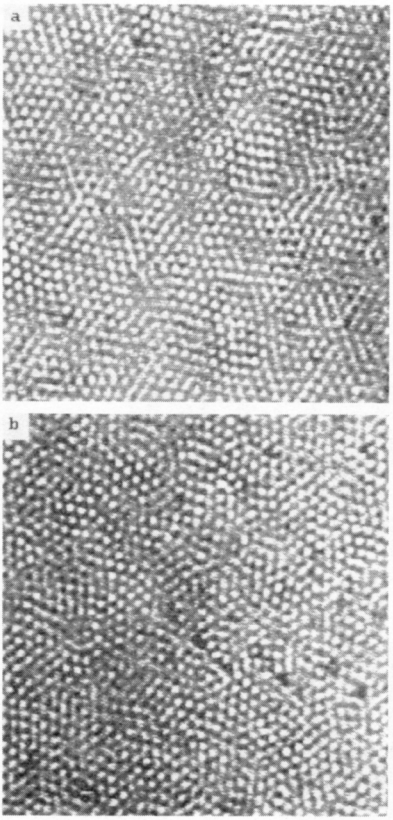

Figure 7 STM images of the incommensurate CDW phase in (*a*) $Nb_{0.07}Ta_{0.93}S_2$ and (*b*) $Nb_{0.1}Ta_{0.9}S_2$.

latter samples exhibit significant disorder with regions of hexagonal order and positional order extending only several lattice constants.

To assess qualitatively the nature of CDW pinning in this system, we first calculate the Nb impurity spacing. In two dimensions, the impurity spacing is $d_i(x) = n_i^{-1/2}$; thus, the average impurity spacings for the x(Nb) = 0.02, 0.04, 0.07, and 0.10 samples are 0.80, 0.57, 0.43, and 0.36 CDW lattice constants, respectively. This estimate shows that there is more than one impurity atom/CDW maxima in the doped samples investigated. Because the STM images indicate that the CDW lattice exhibits order for at least several lattice constants (which will contain many impurities), these results are suggestive of the weak pinning regime described by the FLR model.

Topological Defects

The topology and density of defects can also be assessed by quantitative image analysis (13, 68–70). The quantitative analysis involves defining the location (x, y coordinates) of each CDW maxima and the unique nearest-neighbors in the lattice. Once the lattice points are determined, a sweep-line algorithm (71) is used to construct the Voronoi diagram for the lattice. The Voronoi diagram uniquely defines the nearest-neighbors of all lattice points (72). To illustrate defects in the lattice, we triangulate the Voronoi diagram by drawing "bonds" from all CDW lattice points to their nearest-neighbors. This resulting plot is termed the Delauney triangulation diagram (13, 70). In our CDW system, fully coordinated lattice sites are indicated by six bonds, whereas defects contain a smaller or greater number of bonds. Typical results obtained from the analysis of x(Nb) = 0, 0.02, 0.04, 0.07, and 0.10 samples are shown in Figure 8. In these triangulation diagrams, we have highlighted the defect sites by shading. Inspection of images recorded on pure TaS_2 samples show that the CDW lattice is free of topological defects; i.e., all of the lattice sites are six-fold coordinate (Figure 8*a*). The triangulations explicitly show, however, that the Nb-doped materials have topological defects in the CDW lattice. At low concentrations of impurities, x(Nb) = 0.02 and 0.04, we find that the dislocations consist of five-fold/seven-fold disclination pairs (Figure 8*b*, *c*). Extended defect networks are also obvious in the triangulation data for the x(Nb) = 0.07 and 0.10 samples. These extended topological defects consist of dislocations, vacancies, and free disclinations.

These data have also been used to evaluate the average separation between dislocations. We find that the average spacing between dislocations in the x(Nb) = 0.02, 0.04, 0.07, and 0.1 samples is 12, 8, 5, 3 lattice constants, respectively. As stated above, the average separation between Nb impurity atoms is 0.80, 0.57, 0.43, and 0.26 CDW lattice

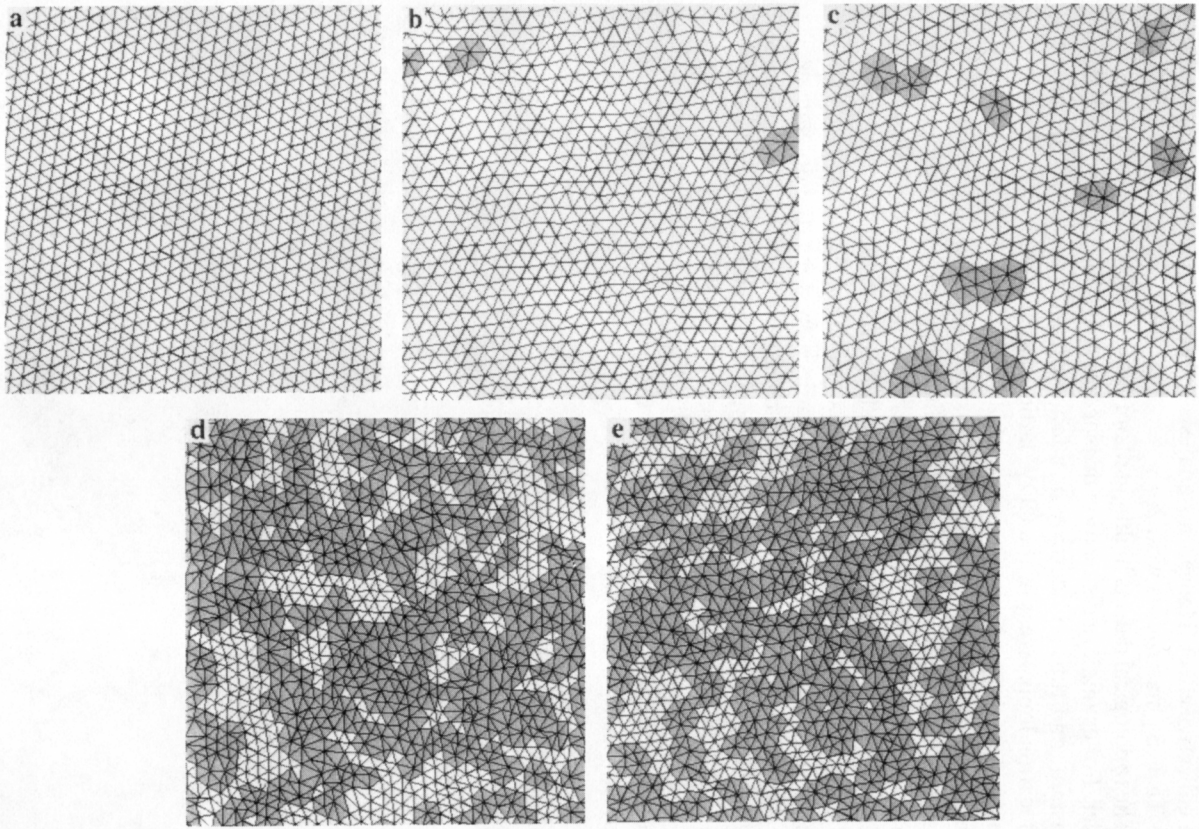

Figure 8 Delauney triangulations of the STM images recorded on $Nb_xTa_{1-x}S_2$ crystals where (*a*), (*b*), (*c*), (*d*), and (*e*) correspond to $x = 0$, 0.02 0.04, 0.07, and 0.10, respectively. Lattice sites that do not have sixfold coordination are highlighted by shading.

constants, respectively. The average spacing between dislocations is thus always greater than the average impurity spacing; that is, impurity pinning is a collective effect. Hence, this analysis shows that CDW pinning in the $Nb_xTa_{1-x}S_2$ materials is weak.

The topological defects highlighted in Figure 8 strongly affect positional order. For example, a dislocation displaces lattice points by about a lattice constant, and thus will destroy positional order on a scale of the size of dislocation loop. Areas of the CDW lattice that are free from dislocations should, however, exhibit a smooth variation in the CDW phase, i.e. the domains in the FLR model. Figure 9 illustrates a typical large scale image, with several phase coherent regions highlighted to demonstrate this important point. This image also shows clearly that the local crystallographic axes of adjacent domains are rotated with respect to one another.

Further analysis of large area images containing different impurity concentrations shows that the area of the ordered regions (the domain size) shrinks as the impurity concentration increases. This behavior follows directly from Equation 10. Importantly, if we take the dislocation separation as the critical length, L_c, using the impurity spacing d_i given above, we find that the calculated value of the FLR pinning parameter ε is ~ 0.1. These results confirm quantitatively that the system is in the weakly pinned regime.

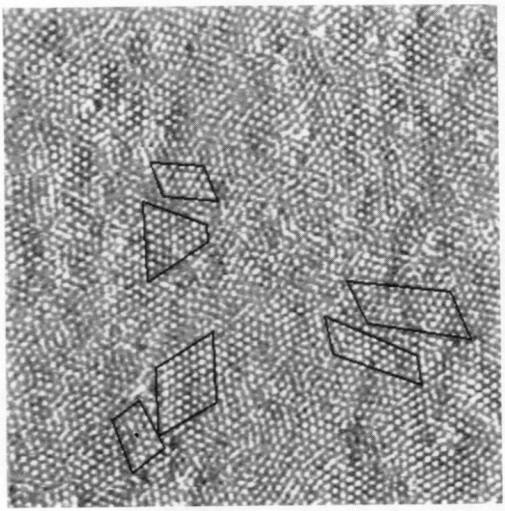

Figure 9 A large area STM image of the incommensurate CDW lattice of a $Nb_{0.07}Ta_{0.93}S_2$ sample. Several adjacent domains containing positionally ordered lattices are highlighted with black lines. Note that adjacent domains are rotated with respect to each other.

Two-Dimensional Order

Above we have characterized the nature of CDW pinning and defects. More generally, it is important to examine the consequences of the disorder produced by weak pinning, because this phenomenon is significant to several important physical systems (73, 74). To quantify disorder, we first examine the structure factor $S(\mathbf{k})$

$$S(\mathbf{k}) = |\rho(\mathbf{k})|^2 \qquad 11.$$

where $\rho(\mathbf{k}) = \int \rho(\mathbf{r}) e^{ik \cdot r}\, d\mathbf{r}$ is the Fourier transform of the number density of lattice points. $S(\mathbf{k})$ provides an average of the structural effects of pinning. Figure 10 presents the results for the Nb-substituted materials. $S(\mathbf{k})$ for pure TaS_2 (not shown) exhibit sharp six-fold symmetric peaks (Bragg peaks). These peaks broaden both radially and angularly as the impurity concentration increases to 0.04. For the $x(\mathrm{Nb}) = 0.07$ and 0.10, the first order Bragg peaks have broadened to form a ring whose intensity has a six-fold modulation. The angular broadening is due to CDW rotations, discussed above. This broadening indicates a loss of orientational order; however, a quantitative measure of the orientational dis-

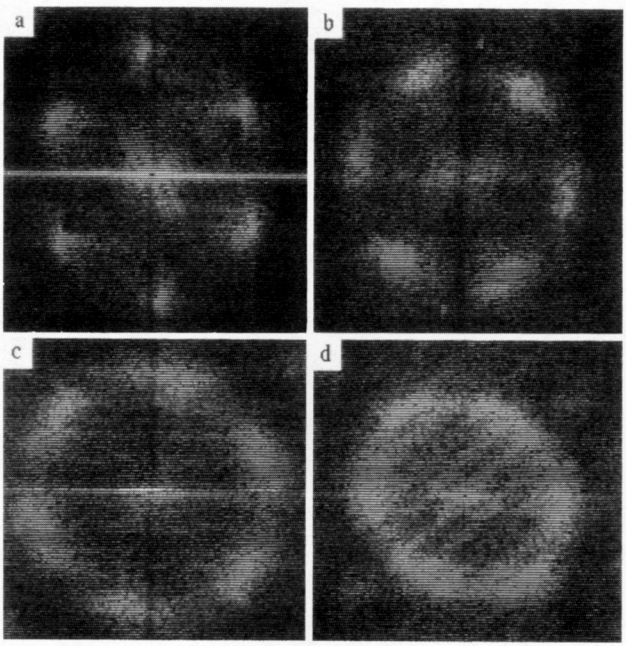

Figure 10 Structure factors corresponding to the CDW lattices of (*a*) $x = 0.02$, (*b*) $x = 0.04$, (*c*) $x = 0.07$, and (*d*) $x = 0.10$ $Nb_xTa_{1-x}S_2$ materials.

order cannot be provided from these $S(\mathbf{k})$ data. In addition, the radial widths of the Bragg peaks indicate that the translational correlation length is short in all of the Nb-doped materials. Notably, our $S(\mathbf{k})$ data are qualitatively similar to the results expected for second order melting transition in two dimensions (11, 69, 70, 73, 74).

To provide a more quantitative measure of the order in this system and how it is affected by impurity pinning, we have systematically investigated the radial distribution, translational correlation, and orientational correlation functions. The radial distribution function is defined as $g(r) = \langle n(r) \rangle / n_o$, where $n(r)$ is the point density at a distance r from the origin of the structure, and n_o is the average density of points. For a general structure, $g(r)$ tends to 1 as r goes to infinity, i.e. the distribution of lattice points at large distances appears uniform. Plots of $g(r)$ determined from STM images of the $Nb_xTa_{1-x}S_2$ materials are presented in Figure 11. For the pure sample, $g(r)$ oscillates strongly out to more than 10 lattice constants. The persistent oscillation indicates that positional order is long range. When the impurity level increases to 0.02 and 0.04, the amplitude of the oscillations in $g(r)$ decreases, and the oscillations die out much more rapidly than in $g(r)$ for the pure material (Figure 11*a–c*). For the $x(\mathrm{Nb}) = 0.07$ or 0.10 materials, the amplitude of the peaks in $g(r)$ is further reduced, and those peaks only persist to the second or third nearest-neighbors. These results indicate that Nb impurity pinning-induced disorder destroys translational order in this CDW system.

The order of the CDW system can be further characterized by calculating the translational and orientational correlation functions. These functions were first introduced by Mermin (75) in his theoretical studies of the positional and orientational order of two-dimensional solids. In two dimensions, the translational correlation function is defined as

$$G_T(\mathbf{r}) = \langle \psi(\mathbf{0}) \psi(\mathbf{r})^* \rangle, \tag{12.}$$

where

$$\psi(\mathbf{r}) = \frac{1}{3} \sum_{i=1}^{3} e^{i\mathbf{G}_i \cdot \mathbf{r}} \tag{12a.}$$

is the translational order parameter for a hexagonal lattice at position $\mathbf{r}$. This order parameter consists of the local Fourier components of the number density of lattice points at reciprocal lattice vectors $\mathbf{G}$. The translational correlation function is equivalent to the Debye-Waller factor, and its Fourier transform gives the structure factor $S(\mathbf{k})$. Thus, it measures how lattice points are correlated positionally in real space.

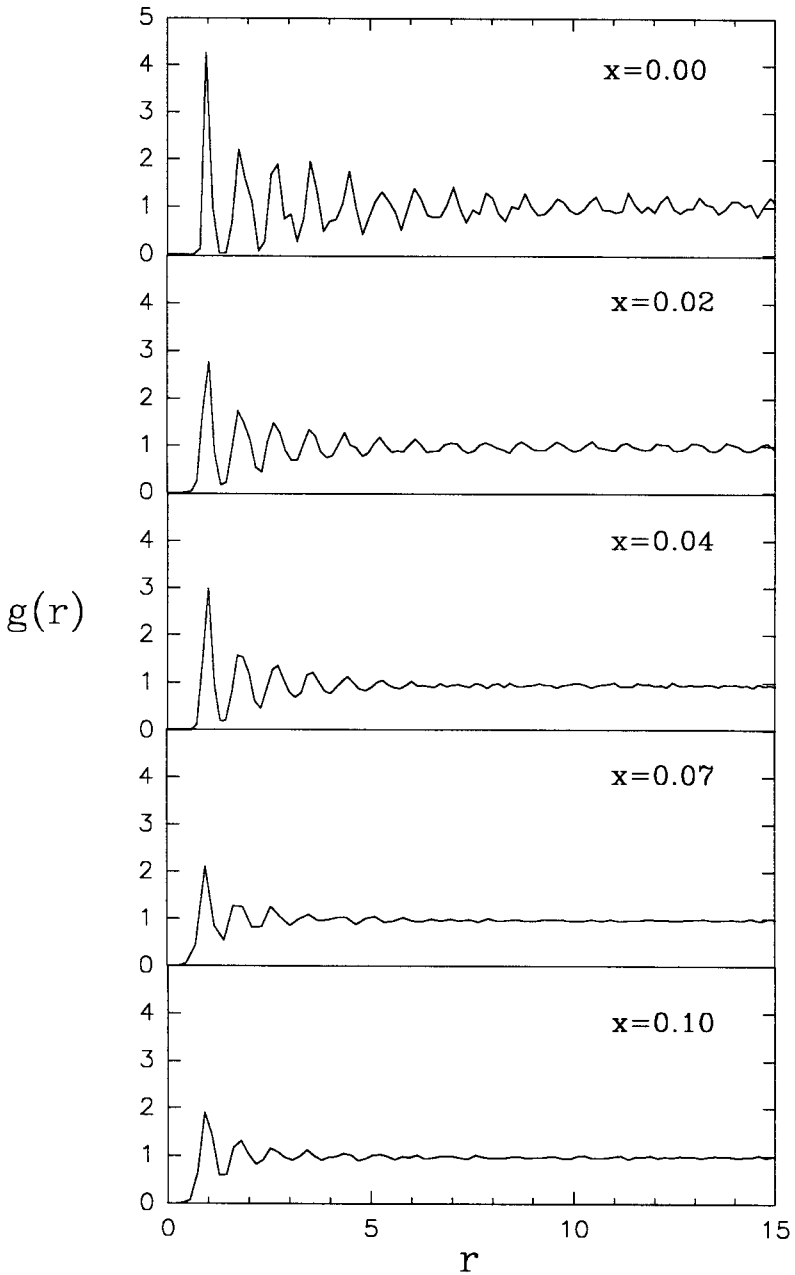

Figure 11 Radial distribution functions for the $Nb_xTa_{1-x}S_2$ materials. The x-axis corresponds to CDW lattice constants.

The orientational correlation function for a two-dimensional lattice with hexagonal symmetry is defined as

$$G_6(\mathbf{r}) = \langle \psi_6(\mathbf{0}) \psi_6(\mathbf{r})^* \rangle, \tag{13.}$$

where

$$\psi_6(\mathbf{r}) = \sum_{i=1}^{nn} e^{i6\theta_{i(\mathbf{r})}} \tag{13a.}$$

is the orientational order parameter at position $\mathbf{r}$. $\theta(\mathbf{r})$ is the local bond angle with respect to a given direction. Bonds correspond to the lines that connect the nearest-neighbors (*nn*) defined by the Voronoi analysis and Delauney triangulation discussed earlier. The sum is over all *nn* bonds of a point at position $\mathbf{r}$. This definition for the orientational correlation function is also valid for liquids, as the average coordination number of a two-dimensional liquid is also six.

It is instructive to examine the general behavior of these correlation functions before we proceed with the analysis of the CDW system. First, translational and orientational order of a crystal lattice are often coupled to one another. For example, a grain boundary rotates the area (volume) of one part of a crystal lattice relative to an adjacent one; this rotation disrupts both translational and orientation order. However, $G_T(\mathbf{r})$ and $G_6(\mathbf{r})$ can exhibit very different dependencies with $\mathbf{r}$. First, theoretical studies have shown that long wavelength phonon fluctuations destroy only translational order in a two-dimensional solid; orientational order will remain long range (75, 76). Secondly, Halperin and Nelson (57, 58) have shown that dislocations affect translational and orientational order differently in two-dimensional crystals: Translational order is destroyed and decays exponentially, whereas orientational order is quasi-long ranged and decays algebraically.

Calculated results for $G_T(\mathbf{r})$ and $G_6(\mathbf{r})$ for the $Nb_xTa_{1-x}S_2$ materials are shown in Figure 12. $G_T(\mathbf{r})$ and $G_6(\mathbf{r})$ decay very slowly over 20 lattice constants for the incommensurate CDW lattice of the pure sample. This quasi-long-range order is indicative of a crystalline state. In contrast, all of the samples that contain Nb impurities exhibit a rapid decay of translational order. This decay in $G_T(\mathbf{r})$ can be fit reasonably well to an exponential of the form $G_T(\mathbf{r}) = \exp(-r/\xi_T)$ where ξ_T is the translational correlation length. The ξ_T's are 7–10, 3–6, 2–3, 1–2 CDW lattice constants for the $x(\text{Nb}) = 0.02$, 0.04, 0.07, and 0.10 samples, respectively. These results demonstrate quantitatively that the dislocations and other defects arising from weak pinning destroy translation order. In contrast, we find that the orientational order decays slowly for the $x(\text{Nb}) = 0.02$ and 0.04

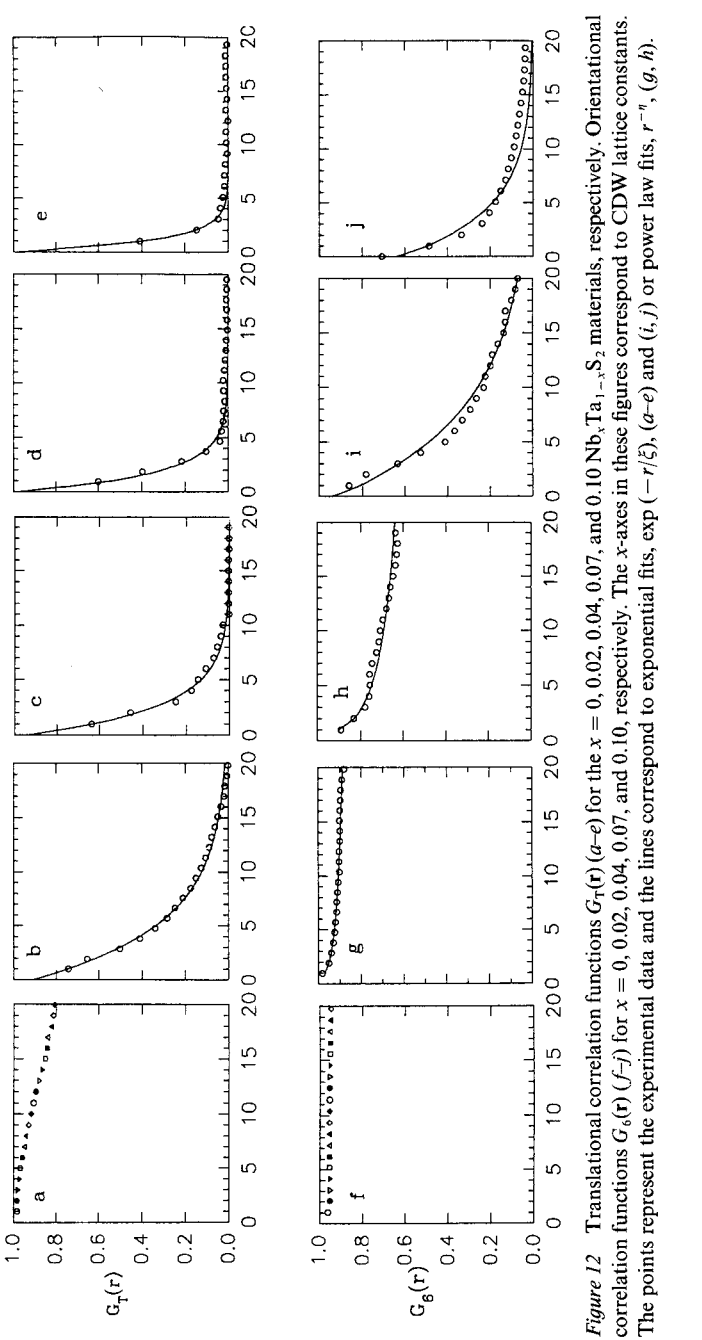

Figure 12 Translational correlation functions $G_T(\mathbf{r})$ (*a–e*) for the $x = 0, 0.02, 0.04, 0.07$, and 0.10 $Nb_xTa_{1-x}S_2$ materials, respectively. Orientational correlation functions $G_6(\mathbf{r})$ (*f–j*) for $x = 0, 0.02, 0.04, 0.07$, and 0.10, respectively. The *x*-axes in these figures correspond to CDW lattice constants. The points represent the experimental data and the lines correspond to exponential fits, $\exp(-r/\xi)$, (*a–e*) and (*i, j*) or power law fits, $r^{-\eta}$, (*g, h*).

samples, although $G_6(\mathbf{r})$ decays rapidly for $x(\mathrm{Nb}) = 0.07$ and 0.10 (Figure 12). If the $x(\mathrm{Nb}) = 0.02$, 0.04, 0.07, and 0.10 $G_6(\mathbf{r})$ data are fit with an exponential, $G_6(\mathbf{r}) = \exp(-r/\xi_6)$, we obtain orientational correlation lengths (ξ_6) of 200, 100, 11, and 5 lattice constants, respectively. A better fit to $G_6(\mathbf{r})$ for $x(\mathrm{Nb}) = 0.02$ and 0.04 is obtained, however, by using an algebraic decay, $G_6(\mathbf{r}) = r^{-\eta}$, with $\eta = 0.03$ and 0.12, respectively.

The simultaneous observation of long-range orientational order and short-range translational order in the $x(\mathrm{Nb}) = 0.02$ and 0.04 samples is strongly suggestive of the hexatic state that was proposed on the basis of theoretical studies of two-dimensional melting driven by topological defects (57, 58). This theory predicts that two-dimensional melting involves two continuous phase transitions. First, a crystalline solid phase that has quasi-long-range translational order and long-range orientational order [$G_T(\mathbf{r}) = r^{-\xi}$; $G_6(\mathbf{r}) \sim 1$] undergoes a second order transition to the hexatic phase that has short-range translational order and quasi-long-range orientational order: $G_T(\mathbf{r}) = \exp(-r/\xi_T)$; $G_6(\mathbf{r}) = r^{-\eta}$. At higher temperature, the hexatic undergoes a second continuous transition to a liquid phase that has short-range translational and orientational order: $G_T(\mathbf{r}) = \exp(-r/\xi_T)$; $G_6(\mathbf{r}) = \exp(-r/\xi_6)$. The results for the CDW phase in $Nb_xTa_{1-x}S_2$ show similar behavior; thus, we suggest that the CDW lattice evolves from crystalline ($x = 0$) through hexatic glass ($x = 0.02$–0.04) to liquid-like ($x > 0.07$) states. We assign the intermediate state to a hexatic glass (versus equilibrium hexatic), because the impurity distribution in these materials is quenched. The fundamental difference between the two-dimensional melting theory and our study is that the topological defects arise from thermal fluctuations in the former and from pinning to a quenched impurity distribution in our work. Because statistical averaging differs for equilibrium versus quenched disorder (62), we have further investigated the similarities of the CDW system to equilibrium melting.

First, we can estimate the power law exponent η by using the relationship $\eta = 9c/\pi$, where c is a fractional area of dislocation cores, derived for dislocations in thermal equilibrium (69). The values of η calculated in this way, 0.02 and 0.13, are in excellent agreement with the values obtained from fits to $G_6(\mathbf{r})$ for $x(\mathrm{Nb}) = 0.02$ and 0.04. This agreement suggests that dislocations arising from impurity pinning are responsible for the decay in orientational correlation. Although the average dislocation spacing (ξ_D) is similar to ξ_T, ξ_D is always larger than ξ_T at the smallest impurity concentration (Table 1). The fact that $\xi_T < \xi_D$ in the $x(\mathrm{Nb}) = 0.02$ samples indicates that factors in addition to dislocations decrease translational order; this observation contrasts the prediction of equilibrium theory. However, we can explain this result (i.e. $\xi_T < \xi_D$) within the context of weak pinning theory. As discussed above, the CDW phase varies smoothly

Table 1 Important length scales in the $Nb_xTa_{1-x}S_2$ CDW system

$Nb_xTa_{1-x}S_2$	d_i	ε_D	ε_T	ε_6	η
$x = 0.02$	0.80	12	7–10	200	0.02
$x = 0.04$	0.57	8	3–6	100	0.13
$x = 0.07$	0.43	5	2–3	11	—
$x = 0.10$	0.36	3	1–2	5	—

The units for d_i, ε_D, ε_T, ε_6 are CDW lattice constants

from $-\pi$ to π in regions separated by dislocations (i.e. within domains). The smooth variation in phase causes small distortions of the CDW lattice positions that reduce the translational order. Indeed, Chudnovsky (77, 78) has explicitly shown how elastic distortions (i.e. smooth variations in the phase versus a singular phase variation at a dislocation) destroy the positional order of weakly pinned lattices. Hence, a combination of the equilibrium melting and weak pinning theories provide a better description of the changes in translational correlation for this metal-substituted CDW system.

Manifestations of Dimensionality

The analysis discussed above indicates that the CDW state in $Nb_xTa_{1-x}S_2$ can be treated as a two-dimensional system. Because dimensionality plays an essential role in determining the physical properties of materials (e.g. the physics of critical phenomena), we examine further the consequences of the dimensionality of a system below.

The CDW pinning theory developed earlier shows that different effects should arise from pinning in systems of different dimensionality. First, domain formation should occur for a weakly pinned CDW for $d < 4$ (47, 48, 66). This prediction for domain formation does not, however, lead to distinguishable criteria in our system. Secondly, the impurity concentration dependence for pinning also varies significantly for systems of different dimensionality. This variation is readily apparent upon examination of the parameter ε in Equation 9. For a one-dimensional CDW chain, $\varepsilon \approx \rho_0 V_o / n_i \kappa \propto n_i^{-1}$. Hence, in a one-dimensional system the pinning should be strong if the impurities are dilute, and pinning should be weak if the impurities are dense. In two dimensions, however, $\varepsilon \approx \rho_0 V_o / \kappa$. This indicates that the pinning strength (weak or strong) should be independent of impurity concentration. Our studies are consistent with this prediction, as the results for the $Nb_xTa_{1-x}S_2$ materials indicate that pinning is weak for $0 \leqslant x \leqslant 0.1$.

As indicated above, melting in two dimensions also differs fundamentally from melting in three dimensions. The solid to liquid phase transition in a three-dimensional solid is an abrupt first order phase transition with discontinuities in the thermodynamic parameters. However, two-dimensional melting is characterized by two continuous phase transitions that are mediated by topological defects. The first transition is from a crystalline solid to a hexatic phase and is caused by paired dislocations unbinding into isolated dislocations. The second transition is from the hexatic phase to a liquid phase and is caused by dislocation unbinding into isolated disclinations. Our investigations of the Nb-doped materials bear a strong resemblance to the theoretical predictions for two-dimensional melting and do not exhibit an abrupt phase transition, based on our analysis of the structural order. However, these systems are clearly not ideal two-dimensional systems, and at least small three-dimensional couplings are expected (i.e. between layers). The effect of interlayer coupling has been considered theoretically by McMillan (64). He argued that weak coupling of the CDW phase between layers will provide three-dimensional stiffness to the CDW and, hence, should not undergo a two-dimensional melting transition. To clarify this issue, it will be necessary to assess experimentally the strength of the interlayer interactions and the three-dimensional stiffness of the CDW. In the future, these parameters could be probed by determining thermodynamic quantities (e.g. heat capacity) and the structure as a function of temperature.

Macroscopic Observables and Microscopic Structure

A central result presented above is the direct elucidation of the structural manifestations of quenched impurity pinning. We have identified three different phases of the pinned IC CDW lattice: crystalline solid, hexatic glass, and a liquid-like state. It is interesting to ask whether there are observable consequences of these novel structural phases. Indeed, we find that these structurally distinct CDW states can be mapped to distinct macroscopic transport behavior. Resistivity data from the pure material exhibit a sharp first-order phase transition. However, in the hexatic glass regime [$x(\mathrm{Nb}) = 0.02$ and 0.04] resistance versus temperature plots show broadened phase transitions. Finally, in the liquid-like state [$x(\mathrm{Nb}) \geqslant 0.07$) no distinct transition is observed in the resistivity data. Thus, the three structurally distinct CDW phases may correspond to true thermodynamic phases. Other physical measurements, such as heat capacity and magnetic susceptibility, should also be carried out to confirm this suggestion. Lastly, we suggest that it will be interesting to study the electric field dependence of electrical transport in the hexatic glass phase. Because dislocations, which have been characterized through our STM

studies, lower the shear stress in a lattice, it may be possible to depin the CDW from the lattice in an electric field. The depinned CDW could slide and provide an additional current carrying pathway (44, 45).

CONCLUDING REMARKS

We have used STM and quantitative image analysis to elucidate systematically CDW pinning and disorder in $Nb_xTa_{1-x}S_2$ solids. Analyses of STM images demonstrate that Nb impurities introduce topological defects into the CDW lattice. Quantitative analysis of the density of dislocations and comparisons of these data with theoretical scaling arguments demonstrate unambiguously that the pinning of the CDW by Nb impurities is weak. In addition, we have shown how pinning affects the translational and orientational order of the two-dimensional CDW lattice. Calculations of the translational and orientational correlation functions suggest that the CDW lattice evolves continuously from a crystalline solid, $x(\mathrm{Nb}) = 0$, to a hexatic glass, $0 < x(\mathrm{Nb}) \leqslant 0.04$, and finally to an amorphous state, $x(\mathrm{Nb}) \geqslant 0.07$. Finally, we have shown that the structural evolution of the CDW lattice with increasing impurity concentration has many analogous features to equilibrium melting in two dimensions, although differences may arise from the quenched disorder and pinning in $Nb_xTa_{1-x}S_2$. $M_xTa_{1-x}S_2$ materials will be ideal systems for future studies, as the impurity concentration and potential can be varied systematically, and the CDW-lattice coupling can be changed through variations in the temperature. Hence, experimental and theoretical investigations of this system will lead to a much deeper understanding of pinning and nonequilibrium disorder in two-dimensional systems. In a more general sense, STM could provide key insight into understanding the microscopic properties of other complex low-dimensional solids (4). Future investigations of such materials will undoubtedly lead to significant advances in our understanding of materials.

ACKNOWLEDGMENT

Support was provided from the National Science Foundation (DMR 89-19201), the Air Force Office of Scientific Research (AFOSR 90-0029), and the Harvard-NSF Materials Research Laboratory.

Literature Cited

1. DiSalvo, F. J. 1992. *Science* 247: 649
2. 1986. *Physics Through the 1990s: Condensed-Matter Physics*. Washington: Natl. Acad. Press. 307 pp.
3. Lieber, C. M., Wu, X. L. 1991. *Acc. Chem. Res.* 24: 170
4. Zhang, Z., Lieber, C. M. 1992. *J. Phys. Chem.* 96: 2030

5. Cheetham, A. K., Day, P. 1987. *Solid State Chemistry: Techniques*. Oxford: Clarendon. 398 pp.
6. Wu, X. L., Zhang, Z., Wang, Y. L., Lieber, C. M. 1990. *Science* 248: 1211
7. Wu, X. L., Zhou, P., Lieber, C. M. 1988. *Nature* 335: 55
8. Wu, X. L., Zhou, P., Lieber, C. M. 1988. *Phys. Rev. Lett.* 61: 2604
9. Chen, H., Wu, X. L., Lieber, C. M. 1990. *J. Am. Chem. Soc.* 112: 3326
10. Wu, X. L., Lieber, C. M. 1989. *J. Am. Chem. Soc.* 111: 2731
11. Dai, H., Chen, H., Lieber, C. M. 1991. *Phys. Rev. Lett.* 66: 3183
12. Wu, X. L., Lieber, C. M. 1990. *Phys. Rev. B* 41: 1239
13. Dai, H., Lieber, C. M. 1992. *Phys. Rev. Lett.* 69: 1576
14. Kelty, S. P., Lieber, C. M. 1989. *J. Phys. Chem.* 93: 5983
15. Kelty, S. P., Lieber, C. M. 1989. *Phys. Rev. B* 40: 5856
16. Zhang, Z., Wang, Y. L., Wu, X. L., Huang, J.-L., Lieber, C. M. 1990. *Phys. Rev. B* 42: 1082
17. Wu, X. L., Wang, Y. L., Zhang, Z., Lieber, C. M. 1991. *Phys. Rev. B* 43: 8729
18. Zhang, Z., Chen, C. C., Lieber, C. M., Morosin, B., Venturini, E. L., Ginley, D. S. 1992. *Phys. Rev. B* 45: 987
19. Zhang, Z., Lieber, C. M. 1992. *Phys. Rev. B* 46: 5845
20. Niu, C., Lieber, C. M. 1992. *J. Phys. Chem.* 96: 3419
21. Binnig, G., Rohrer, H. 1987. *Angew. Chem. Int. Ed. Engl.* 26: 606
22. Hansma, P. K., Tersoff, J. 1987. *J. Appl. Phys.* 61: R1
23. Kuk, Y., Silverman, P. J. 1989. *Rev. Sci. Instrum.* 60: 165
24. Avouris, P. 1990. *J. Phys. Chem.* 94: 2246
25. Griffith, J. E., Kochanski, G. P. 1990. *Annu. Rev. Mater. Sci.* 20: 194
26. Hamers, R. J. 1989. *Annu. Rev. Phys. Chem.* 40: 351
27. Tersoff, J., Hamann, D. R. 1985. *Phys. Rev. B* 31: 805
28. Lang, N. D. 1986. *Phys. Rev. Lett.* 56: 1164
29. Selloni, A., Carnevalli, P., Tosatti, P. E., Chen, C. D. 1986. *Phys Rev. B* 33: 5770
30. Tersoff, J. 1990. *Phys. Rev. B* 41: 1235
31. Chen, C. J. 1990. *Phys. Rev. Lett.* 65: 448
32. Bardeen, J. 1963. *Phys. Rev. Lett.* 6: 57
33. Balchin, A. A. 1976. In *Crystallography and Crystal Chemistry of Materials With Layered Structures*, ed. F. Levy, 2: 1. Boston: Reidel. 369 pp.
34. DiSalvo, F. J. 1977. In *Electron-Phonon Interactions and Phase Transitions*, ed. T. Riste, p. 107. New York: Plenum
35. Wilson, J. A., DiSalvo, F. J., Mahajan, S. 1975. *Adv. Phys.* 24: 117
36. Withers, R. L., Wilson, J. A. 1986. *J. Phys. C* 19: 4809
37. Coleman, R. V., Drake, B., Hansma, P. K., Slough, G. 1985. *Phys. Rev. Lett.* 55: 394
38. Wu, X. L., Lieber, C. M. 1989. *Science* 243: 1703
39. Wu, X. L., Lieber, C. M. 1990. *Phys. Rev. Lett.* 64: 1150
40. Thomson, R. E., Walter, U., Ganz, E., Clarke, J., Zettl, A., et al. 1988. *Phys. Rev. B* 38: 10734
41. Giambattista, B., Slough, C. G., McNairy, W. W., Coleman, R. V. 1990. *Phys. Rev. B* 41: 10082
42. Slough, C. G., McNairy, W. W., Coleman, R. V., Garnaes, J., Prater, C. B., Hansma, P. K. 1990. *Phys. Rev. B* 42: 9255
43. Burk, B., Thomson, R. E., Zettl, A., Clarke, J. 1991. *Phys. Rev. Lett.* 66: 3040
44. Gruner, G. 1988. *Rev. Mod. Phys.* 60: 1129
45. Gruner, G., Zettl, A. 1985. *Phys. Rep.* 119: 117
46. DiSalvo, F. J., Wilson, J. A., Bagley, B. G., Waszczak, J. V. 1975. *Phys. Rev. B* 12: 2220
47. Fukuyama, H., Lee, P. A. 1978. *Phys. Rev. B* 17: 535
48. Lee, P. A., Rice, T. M. 1979. *Phys. Rev. B* 19: 3970
49. Coppersmith, S. N. 1990. *Phys. Rev. Lett.* 65: 1044
50. Tucker, J. R. 1989. *Phys. Rev. B* 40: 5447
51. Bardeen, J. 1990. *Phys. Rev. Lett.* 64: 2297
52. Sweetland, E., Tsai, C.-Y., Wintner, B. A., Brock, J. D., Thorne, R. E. 1990. *Phys. Rev. Lett.* 65: 3165
53. Tucker, J. R. 1990. *Phys. Rev. Lett.* 65: 270
54. Gill, J. C. 1990. *Phys. Rev. Lett.* 65: 271
55. Thorne, R. E., McCarten, J. 1990. *Phys. Rev. Lett.* 65: 273
56. Kosterlitz, J. M., Thouless, D. J. 1973. *J. Phys. C* 6: 1181
57. Halperin, B. I., Nelson, D. R. 1978. *Phys. Rev. Lett.* 4: 121
58. Nelson, D. R., Halperin, B. I. 1979. *Phys. Rev. B* 19: 2457
59. Young, A. P. 1979. *Phys. Rev. B* 19: 1985
60. Nelson, D. R. 1983. In *Phase Transitions and Critical Phenomena*, ed. C. Domb, J. L. Lebovitz, 7: 1. London: Academic
61. Strandburg, K. J. 1988. *Rev. Mod. Phys.* 60: 161

62. Ma, S.-K. 1976. *Modern Theory of Critical Phenomena* Reading: Benjamin/Cummings
63. Frohlich, H. 1954. *Proc. R. Soc. A* 223: 296
64. McMillan, W. L. 1975. *Phys. Rev. B* 12: 1187
65. Matsukawa, H., Takayama, H. 1987. *J. Phys. Soc. Jpn.* 56: 1507
66. Imry, Y., Ma, S.-K. 1975. *Phys. Rev. Lett.* 35: 1399
67. Nabarro, F. R. N. 1967. *Theory of Dislocations*. New York: Dover. 821 pp.
68. Dai, H., Lieber, C. M. 1993. *J. Phys. Chem.* 97: 2362
69. Nelson, D. R., Rubinstein, M., Spaepen, F. 1982. *Philos. Mag. A* 46: 105
70. Murray, C. A., Sprenger, W. O., Wenk, R. A. 1990. *Phys. Rev. B* 42: 688
71. Fortune, S. 1987. *Algorithmica* 2: 153
72. Voronoi, G. F. 1908. *J. Reine Agnew. Math.* 134: 198
73. Murray, C. A., Gammel, P. L., Bishop, D. J., Mitzi, D. B., Kapitulnik, A. 1990. *Phys. Rev. Lett.* 64: 2312
74. Seshadri, R., Westervelt, R. M. 1991. *Phys. Rev. Lett.* 66: 2774
75. Mermin, N. D. 1968. *Phys. Rev.* 176: 250
76. Peierls, R. E. 1923. *Helv. Phys. Acta* 7: 81
77. Chudnovsky, E. M. 1989. *Phys. Rev. B* 40: 11355
78. Chudnovsky, E. M. 1991. *Phys. Rev. B* 43: 7831